# DEVELOPMENT AND VALIDATION OF NEW CRYOGENIC CAVITATION MODEL FOR ROCKET TURBOPUMP INDUCER

**Naoki TANI**
JAPAN Aerospace Exploration Agency
Tsukuba, Ibaraki, JAPAN

**Shin-ichi TSUDA**
JAPAN Aerospace Exploration Agency
Tsukuba, Ibaraki, JAPAN

**Nobuhiro YAMANISHI**
JAPAN Aerospace Exploration Agency
Tsukuba, Ibaraki, JAPAN

**Yoshiki YOSHIDA**
JAPAN Aerospace Exploration Agency
Kakuda, Miyagi, JAPAN

## ABSTRACT

Cryogenic fluids, such as liquid hydrogen and oxygen, are often used as rocket propellants, and it is known that a suction performance of turbopump inducer in cryogenic fluid is improved due to 'Thermodynamic effect'. Thermodynamic effect can be explained by temperature decrease inside a cavity region arising from the latent heat absorption. For better understanding of suction performance of inducer, CFD is one of the most important tools. Computational cost is important for CFD which is used in the design phase, and a number of governing equations must be small. Therefore, in the present study, cryogenic cavitation model without energy equation was established. The present model considers that temperature decrease due to latent heat absorption is analytically estimated. Validation calculations were carried out for blunt headforms and hydrofoils for water cavitation and a two-dimensional blunt body, Laval nozzles and inducers for cryogenic fluids. According to these validation calculations, good agreement can be observed, and this result indicates that this model is applicable for cryogenic inducer design.

## INTRODUCTION

Cryogenic fluids, such as liquid hydrogen, oxygen and methane, are often used as a high performance rocket engine propellant. To feed and pressurize a large amount of propellant, gas turbine driven pump, which is called turbopump, is used (Fig.1), and radial impeller is usually used as a main pump. Rotational speed of turbopump should be high to minimize the pump size and mass, therefore, occurrence of cavitation cannot be avoidable. Therefore, inducer (Fig.1 right) is usually adopted at the upstream of the main pump, and its suction performance, inducer H-σ characteristic curve, is important for inducer design.
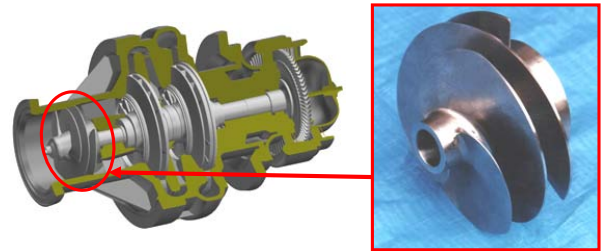


**Figure 1:** The turbopump for the rocket engine and the inducer

It is well known that suction performance is improved in a cryogenic fluid[1]. This performance improvement is derived from latent heat absorption, and this effect is called thermodynamic effect. Deshpande et al.[2] and Tokumasu et al.[3] considered heat exchange at the interface between liquid and sheet cavitation, and both reports shows that sheet cavity length is reduced by the thermodynamic effect. Tani and Nagashima[4] used bubbly cavitation model and compared cavitation lift performance around a single hydrofoil. The reports revealed that lift performance improvement can be solved by CFD, and not only cavity length but also cavity thickness is influenced by the thermodynamic effect. CFD by Hosangadi and Ahuja[5] used fluid property database, and their result clearly shows inducer suction performance improvement, and void fraction becomes smaller in the cryogenic fluid. Most of these researches consider energy equation to handle latent heat absorption. However, solving additional equation requires much computational cost compared to the conventional water cavitation CFD, which does not solve energy equation. Computational cost should be small especially for a use of design phase.

In the present study, cryogenic cavitation model without energy equation is established. This model obtains temperature change analytically, and combines this temperature difference with bubbly cavitation model. Validation simulations were done on axisymmetric blunt bodies, hydrofoils, a two-dimensional

blunt wing, Laval nozzles and inducers. Working fluid for blunt bodies and hydrofoils are water, and for the other objects are cryogenic fluids such as liquid nitrogen, hydrogen and methane.

## CAVITATION MODEL

A lot of cavitation models are proposed, and most of them are divided into two groups, the one is sheet cavitation model[2, 3], and the other is bubbly cavitation model[4, 5]. However, according to the numerical study by Frikha et al. [6], there is little difference between these models if these numerical models are properly validated and tuned the model coefficients. Almost all of these studies are done on water cavitation, and there are few references and models on cryogenic cavitation. As the first step of the present study, cavitation model for cryogenic fluid is established in this section.

There are few observation experiments since a handling of cryogenic fluid is difficult. Hord[7] and Niiyama[8] visualized cryogenic cavitation, and, according to their results, cryogenic cavitation seems to be consisted by tiny bubbles. It is necessary to clarify that cryogenic cavitation is really consisted by bubbles, but, in the present study, it is assumed that cryogenic cavitation is consisted by a cluster of tiny bubbles.

It is widely known that single bubble motion is governed by the Rayleigh-Plesset equation.

$$R\frac{d^2R}{dt^2}+\frac{3}{2}\left(\frac{dR}{dt}\right)^2=\frac{P_{sat}-P}{\rho_{liq}} \tag{1}$$

Usually, time scale of a bubble is much smaller than that of the surrounding fluid, therefore, the first term is often neglected, and simplified Rayleigh-Plesset equation is widely used for cavitation model for CFD.

$$\frac{dR}{dt}=-sign(P-P_{sat})\sqrt{\frac{2}{3}\frac{|P-P_{sat}|}{\rho_{liq}}} \tag{2}$$

Relation between void fraction, bubble number density and bubble radius can be described as follows.

$$\alpha=N\cdot\frac{4}{3}\pi R^3 \tag{3}$$

Differentiate the above equation with respect to time 't', and using the relation between bubble surface area and radius, equation (3) can be described into follows.

$$\frac{d\alpha}{dt}=N\cdot S\frac{dR}{dt} \tag{4}$$

Presently, N is assumed to be constant. Void fraction can also be described by using bubble surface area and radius.

$$\alpha=\frac{N}{3}SR \tag{5}$$

Eliminating N, S and R in equation (4) by using equation (2), (3) and (5), following void fraction equation can be obtained.

$$\frac{d\alpha}{dt}=-sign(P-P_{sat})\cdot\frac{3\alpha}{R}\sqrt{\frac{2}{3}\frac{|P-P_{sat}|}{\rho_{liq}}} \tag{6}$$

Detailed description about above procedure is also described by Singhal, et al.[9]. The right hand side of the equation (6) has singularity at fully liquid phase since both α and R become zero, therefore, some special treatment is required. Presently, relation between critical bubble radius and pressure[12] is used.

$$R\propto\frac{\sigma_S}{|P_{sat}-P|} \tag{7}$$

Most of the cavitating flow is high Reynolds number flow, flow shear stress is stronger than surface tension, and it can be negligible.

$$R\propto\frac{1}{|P_{sat}-P|} \tag{8}$$

Using equation (8), bubble radius at the denominator in equation (6) can be eliminated.

$$\frac{d\alpha}{dt}=-C(P-P_{sat})\cdot\alpha\sqrt{\frac{2}{3}\frac{|P-P_{sat}|}{\rho_{liq}}} \tag{9}$$

The right hand side of above equation becomes zero if α=0, and cavitation does not occur even a pressure is enough low. Therefore, the same assumption by Singhal et al.[9] were made. They assumed that phase change rate should be proportional to the volume fraction, and mass fraction change by vapor generation/condensation rates are obtained in terms of vapor mass fraction.

$$\frac{d\chi\rho_m}{dt}=\begin{cases}-C_e(P-P_{sat})\cdot(1-\chi)\rho_{vap}\sqrt{\frac{2}{3}\frac{|P-P_{sat}|}{\rho_{liq}}} & (if\ P<P_{sat})\\ -C_c(P-P_{sat})\cdot\chi\rho_{liq}\sqrt{\frac{2}{3}\frac{|P-P_{sat}|}{\rho_{liq}}} & (if\ P<P_{sat})\end{cases} \tag{10}$$

As a result, conservation equation of cavitation vapor is described as follows.

$$\frac{d(\chi\rho_m)}{dt}+\nabla(\chi\rho_m\cdot\mathbf{u})=R_e-R_c \tag{11}$$

$R_e$ and $R_c$ are evaporation and condensation rate, respectively.

$$R_e=\begin{cases}-C_e(P-P_{sat})\cdot(1-\chi)\rho_{vap}\sqrt{\frac{2}{3}\frac{|P-P_{sat}|}{\rho_{liq}}} & (if\ P<P_{sat})\\ 0 & (if\ P<P_{sat})\end{cases} \tag{12}$$

$$R_c=\begin{cases}0 & (if\ P<P_{sat})\\ -C_c(P-P_{sat})\cdot\chi\rho_{liq}\sqrt{\frac{2}{3}\frac{|P-P_{sat}|}{\rho_{liq}}} & (if\ P<P_{sat})\end{cases} \tag{13}$$

The equation described above does not consider latent heat absorption, which is important for cryogenic cavitation. Ideal temperature depression by heat absorption can be described as follows.

$$\Delta T^*=\frac{\rho_{liq}L}{\rho_{vap}C_{Pliq}} \tag{14}$$

And a ratio between ΔT* and real temperature difference is defined as B-factor.

$$B=\frac{\Delta T}{\Delta T^*} \tag{15}$$

The B-factor is measured by a lot of experiments[for example, 7, 11]. The B-factor of ideal gas-liquid mixture is expressed by the following equation[10].

$$B=\frac{\alpha}{1-\alpha} \tag{16}$$

As a result, temperature difference of gas-liquid mixture flow by latent heat absorption can be described as follows.

$$\Delta T = \frac{\alpha}{1-\alpha}\frac{\rho_{liq}L}{\rho_{vap}C_{Pliq}} \tag{17}$$

If pressure and temperature is locally equilibrium, saturation pressure change by latent heat absorption becomes

$$\Delta P_L = -\frac{\alpha}{1-\alpha}\frac{\rho_{liq}L}{\rho_{vap}C_{Pliq}}G_{sat} \tag{18}$$

In addition to the latent heat absorption, turbulence effect to the cavitation should be considered. Singhal, et al.[9] uses apparent saturation pressure increases by turbulent tiny vortex core.

$$\Delta P_{turb} = 0.195\rho_m k \tag{19}$$

Final cavitation model equation can be obtained by equation (11),(12),(13), (18) and (19).

$$\frac{d(\chi\rho_m)}{dt} + \nabla(\chi\rho_m \cdot \mathbf{u}) = R_e - R_c \tag{20}$$

where

$$R_e = \begin{cases} -C_e(P-P_{sat})\cdot(1-\chi)\rho_{vap}\sqrt{\frac{3}{2}\frac{|P-P_{vap}|}{\rho_{liq}}} & (if\ P < P_{sat}) \\ 0 & (if\ P < P_{sat}) \end{cases} \tag{21}$$

$$R_c = \begin{cases} 0 & (if\ P < P_{sat}) \\ -C_c(P-P_{sat})\cdot\chi\rho_{liq}\sqrt{\frac{3}{2}\frac{|P-P_{vap}|}{\rho_{liq}}} & (if\ P < P_{sat}) \end{cases} \tag{22}$$

$$P_{vap} = P_{satref} - \frac{\alpha}{1-\alpha}\frac{\rho_{vap}}{\rho_{liq}}\frac{L}{C_{Pliq}}G_{sat} + 0.195\rho_m k \tag{23}$$

$C_e$ and $C_c$ are model constants and these values are determined in the follows section. The second and third terms in right hand side of equation (23) represents latent heat absorption and turbulence effect, respectively. The energy conservation equation is not solved since temperature difference is modeled in equation (23). $P_{satref}$ is a reference saturation pressure, and this value is usually set to saturation pressure at the inlet temperature. In order to distinguish the present cavitation model, this model is named "Critical Radius Model".

## CFD SOLVER AND MODEL CONSTANTS

In this section, CFD solver and models were mentioned. The primary target of the present model is to be used for design phase, therefore, a commercial solver FLUENT6.3.26 was used, and Critical Radius Model is implemented by using User Defined Function (UDF). Steady SIMPLE method is used as a flow solver in the most validation cases, and some unsteady simulations were also done. Spacial accuracy of advection is second order upwind method. Turbulence model for the present study is a RNG k-ε model since this model shows good quantitative agreement in a lot of other problems. To reduce total grid number, non-equilibrium wall function is used in all cases.

As the first step, model constants $C_e$ and $C_c$ must be determined. Axisymmetric body with spherical headform[13] was chosen as a comparison object. Computational grid is shown in Fig.2. The calculation is done in axisymmetric two-dimensional CFD, and a total grid number is 7000 cells. Fluid property is shown in Table 1. There are two parameters in the present cavitation model, $C_e$ and $C_c$. The critical radius model greatly refers to the study by Singhal et al[9], and they set $C_c$

half value of $C_e$. Therefore, the same manner was used in the present study.

$$C_c = \frac{1}{2}C_e \tag{24}$$

Figure 3 shows pressure distribution comparison at σ=0.3. The $C_e$ value is large, the computation is too unstable to show reasonable result. According to the Fig.3, $C_e$=0.6 show good agreement to the experimental pressure distribution, and this value seems to be the most appropriate value. Therefore, model constant becomes as follows.

$$C_e = 0.6 \qquad and \qquad C_c = 0.3 \tag{25}$$

Pressure distribution at lower cavitation number is shown in Fig. 4. Good agreement can be observed, therefore, the values in Eq.(25) considered to be appropriate, and these values are used in the follows validation calculations.
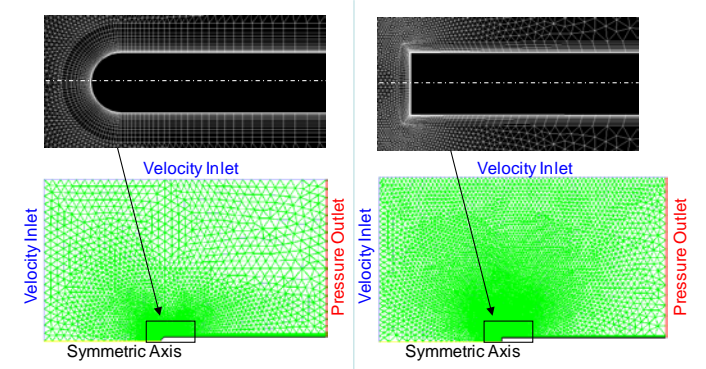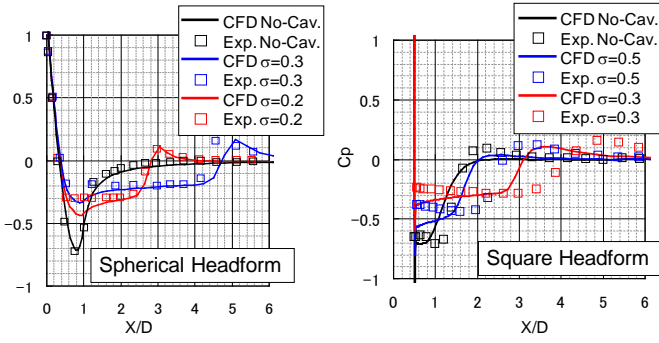


**Figure 2:** Computational grid of axisymmetric body Left: Spherical headform. Right: Square headform

**Table 1:** Fluid property for water calculation

|  | Liquid Phase | Vapor Phase |
|---|---|---|
| Density [kg/m3] | 998.2 | 0.01435 |
| $C_P$[J/kg/K] | 4180. |  |
| Viscosity [Pa s] | $1.002 \times 10^{-3}$ | $9.640 \times 10^{-6}$ |
| Latent Heat [J/kg] | $2.499 \times 10^{6}$ | |
| $G_{sat}$[Pa/K] | 187.9 | |
| $P_{sat}$[Pa] | 2991. | |
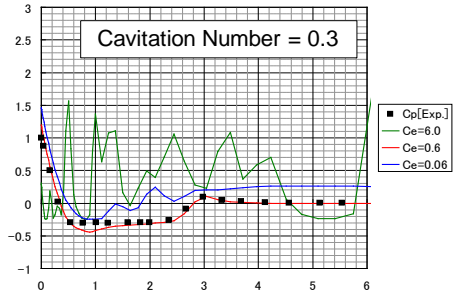


**Figure 3:** Model constant $C_e$ dependency on pressure distribution around the spherical headform

**Figure 4:** Pressure distribution comparison around spherical and square headform



**Figure 5:** Shape and computational grid of Clark-Y and NACA0015 Hydrofoil



**Figure 6:** Lift and drag coefficient change of Clark-Y

## VALIDATION IN WATER

The first step of the validation should be done by water cavitation. It should be noted that present Critical radius model assumes bubbly flow, and sheet cavitation is not suitable to simulate with the present model since void fraction is quite high. Such a high void fraction is out of range from the present model equation, but validation at outside of the appropriate region should be done at the first step in any computational model to clarify its limit. Presently, two objects were chosen as the validation object.

The first object is a blunt body with square headform. The computational grid is also shown in Fig. 2, and this grid has 15000 cells. Fluid property is the same as the spherical headform, which is listed in Table 1. Figure 4 shows pressure distribution comparisons. As mentioned before, computational results of spherical headform show good agreement between experimental and numerical results, but agreement of square headform is poor. In square headform, a large separation occurs at the edge of the headform, and wall function is not suitable for such a large separating flow. The results for square headform indicate that this cavitation model is not appropriate for cavitating flow with strong separation, and the present model should be used for non-separating or weak separating flow, which usually shows good agreement by RANS simulation.

The second objects are hydrofoils. The one hydrofoil is Clark-Y section [14] which is shown in Fig.5. Usually, Strong unsteady cavitation called cloud cavitation is often observed in the past experiments, therefore, unsteady calculations were carried out. Schnerr[15] shows that turbulent viscosity should be modified as follows.
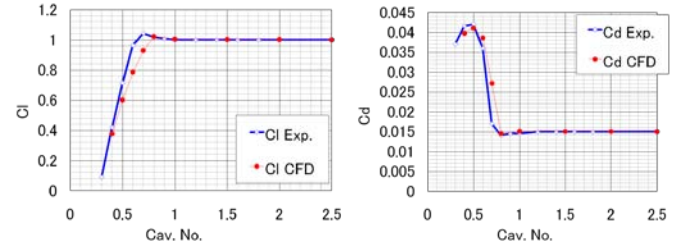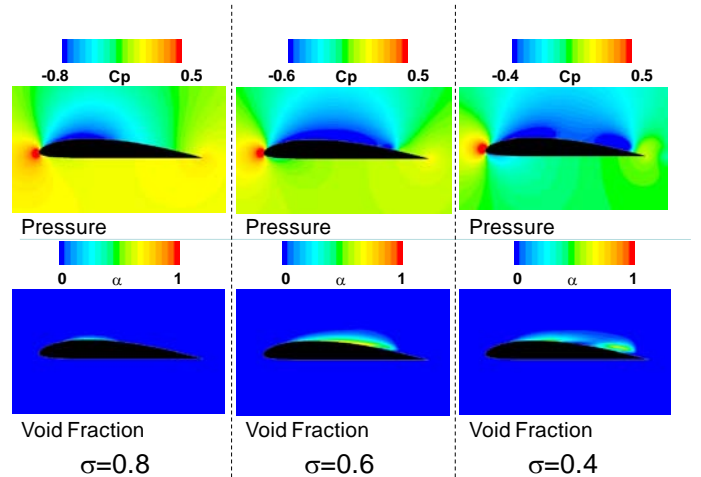
$$\mu_{turb} = f \cdot \mu_{turbke} \tag{22}$$

Where,

$$f = \frac{\rho_{vap}}{\rho_m} + \left| \frac{\rho_{vap} - \rho_m}{\rho_{liq} - \rho_{vap}} \right|^{1000} \frac{\rho_{liq} - \rho_{vap}}{\rho_m} \tag{23}$$
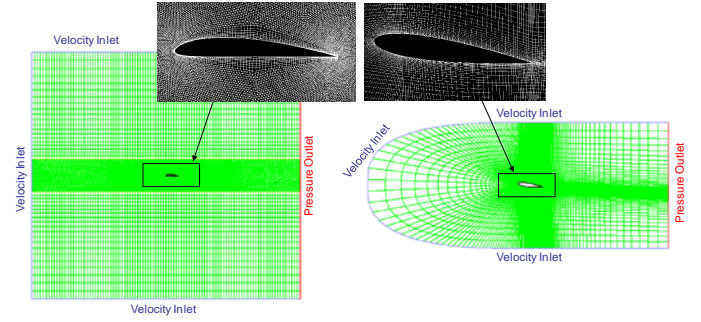


**Figure 7:** Instantaneous pressure and void fraction contour around Clark-Y

In the present calculation, the above modification was applied. Fluid property is the same as Table.1. Figure 6 shows lift and drag coefficient change against cavitation number. Experimental result shows laminar-turbulent transition occurs, however, present simulation assumes fully turbulent flow. Therefore, It should be noted that drag coefficient is modified to adjust above laminar-turbulence difference. The comparison of Fig.6 shows good agreement, and drag increase at the breakdown point is properly calculated. Figure 7 shows instantaneous pressure and void fraction contours, and cloud cavitation shedding from near the trailing edge can be observed at low cavitation number. The second hydrofoil is NACA0015, which grid is also shown in Fig.5. This profile has been calculated in a lot of researches, but showing quantitative agreement is difficult compared to the Clark-Y hydrofoil. Angle of attack and chord length are 8 degree and 0.15m, respectively,

and inlet velocity is set to 8m/s, the same condition as Ref. [16]. The same turbulent viscosity modification was applied to the NACA0015 calculation, since strong cloud cavitation shedding was also observed in the experiment. Fluid property is the same as Table.1. Lift and drag coefficient comparison is shown in Fig.8. The drag coefficient change shows good agreement, however, lift coefficient drop by CFD occurs higher cavitation number compared to the experimental result. A strong cloud cavity shedding occurs at this disagreement region, and this result shows that it is difficult to show quantitative agreement of pressure distribution at strong unsteady cavitating flowing region. Figure 9 shows cavity shape comparison. This comparison show that overall cavity shape is similar, but sheet cavitation from the leading edge cannot captured in the simulation. The present model is based upon a bubbly flow modeling, therefore, sheet cavity cannot be properly simulated. Another interested point is a frequency of cloud cavitation shedding. Figure 10 shows Strouhal number of cloud cavitation. A definition of Strouhal number is as follows[16].

$$F_{ST} = \frac{F \cdot L_{CAV}}{U_{inlet}\sqrt{1+\sigma}} \tag{24}$$

According to the experimental study[16], Strouhal number becomes around 0.1-0.2 by using the above definition. Figure 10 shows the Strouhal number change against cavitation number, and this plot shows that Strouhal number of both profiles becomes around 0.2. This result shows that a large structure of cavitating flow can be simulated by using the present cavitation model.
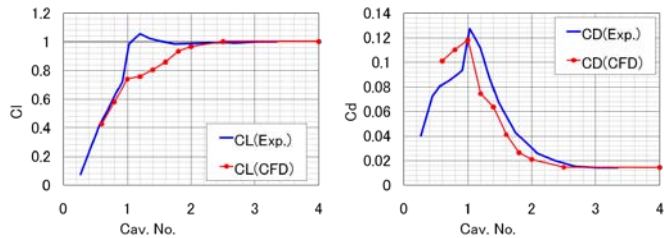


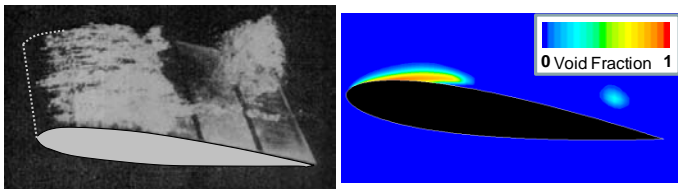**Figure 8:** Lift and drag coefficient change of NACA0015



**Figure 9:** Cavity shape comparison of NACA0015 at σ=1.2. Experimental result is from Ref. [20]
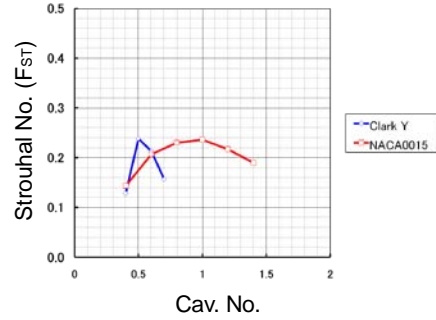


**Figure 10:** Strouhal number of the cloud cavitation by CFD

In summary, the present cavitation model shows good agreement in the spherical headform and the Clark-Y hydrofoil. On the contrary, quantitative agreement is poor with the square headform and the NACA0015 hydrofoil. A difference is that there is no strong separation region or large scale cloud cavitation shedding in the former two objects. This means that the present model is suitable for no-separation or weak-separation flow, which is suitable flow for RANS simulation. Cavity shape show good agreement, but sheet cavitation cannot be simulated since the present model assumes that cavitation is consisted by a lot of tiny bubbles.

## CRYOGENIC FLOW SIMULATION

The second step is a validation in cryogenic fluids, such as liquid nitrogen. Validation objects are two-dimensional blunt wing by Hord[7] and Laval nozzle by Simoneau[17].

The shape and grid of two-dimensional wing are shown in Fig.11. Pressure and temperature distribution around the leading edge is measured in this experiment. In the experiment by Hord, liquid nitrogen, oxygen and hydrogen are used as a working fluid. Presently, liquid nitrogen and hydrogen were chosen, since fluid property of liquid oxygen is similar to that of liquid nitrogen. Fluid properties are listed in the table 2. Figure 12 shows pressure distribution comparison between experiments and calculations, and each comparison shows good agreement. Pressure, void fraction and temperature difference are shown in Fig.13. In the present model, temperature is not directly solved, therefore, temperature difference is evaluated eq.(17). Temperature decrease is about 1 to 2K, but void fraction distribution is different between liquid nitrogen and liquid hydrogen.
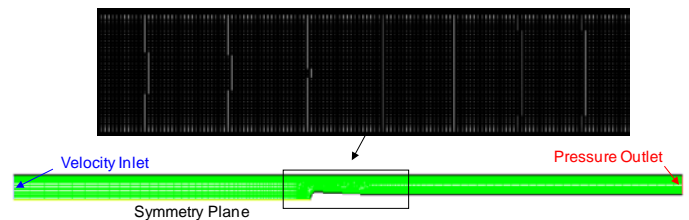


**Figure 11:** Shape and computational grid of two-dimensional wing

5

**Table 2:** Fluid property for cryogenic fluid

RUN 248C: Liquid Hydrogen 20.5K

| | Liquid Phase | Vapor Phase |
|---|---|---|
| Density [kg/m3] | 70.9 | 1.38 |
| $C_P$[J/kg/K] | $1.06 \times 10^4$ | |
| Viscosity [Pa s] | $1.25 \times 10^{-5}$ | $1.13 \times 10^{-6}$ |
| Latent Heat [J/kg] | $4.49 \times 10^5$ | |
| $G_{sat}$[Pa/K] | 30680. | |
| $P_{sat}$[Pa] | $1.08 \times 10^5$ | |

RUN 255C: Liquid Hydrogen 22.0K

| | Liquid Phase | Vapor Phase |
|---|---|---|
| Density [kg/m3] | 69.2 | 2.00 |
| $C_P$[J/kg/K] | $1.10 \times 10^4$ | |
| Viscosity [Pa s] | $1.12 \times 10^{-5}$ | $1.24 \times 10^{-6}$ |
| Latent Heat [J/kg] | $4.46 \times 10^5$ | |
| $G_{sat}$[Pa/K] | 41400. | |
| $P_{sat}$[Pa] | $1.64 \times 10^5$ | |

RUN 293A: Liquid Nitrogen 78.0K

| | Liquid Phase | Vapor Phase |
|---|---|---|
| Density [kg/m3] | 806. | 4.95 |
| $C_P$[J/kg/K] | $2.07 \times 10^3$ | |
| Viscosity [Pa s] | $1.48 \times 10^{-4}$ | $5.55 \times 10^{-6}$ |
| Latent Heat [J/kg] | $1.98 \times 10^5$ | |
| $G_{sat}$[Pa/K] | 12700. | |
| $P_{sat}$[Pa] | $1.09 \times 10^5$ | |

RUN 290C: Liquid Nitrogen 83.0K

| | Liquid Phase | Vapor Phase |
|---|---|---|
| Density [kg/m3] | 69.2 | 2.00 |
| $C_P$[J/kg/K] | $1.58 \times 10^3$ | |
| Viscosity [Pa s] | $1.37 \times 10^{-4}$ | $5.81 \times 10^{-6}$ |
| Latent Heat [J/kg] | $1.91 \times 10^5$ | |
| $G_{sat}$[Pa/K] | 19100. | |
| $P_{sat}$[Pa] | $1.89 \times 10^5$ | |



**Figure 12:** Pressure distribution comparison around two-dimensional wing
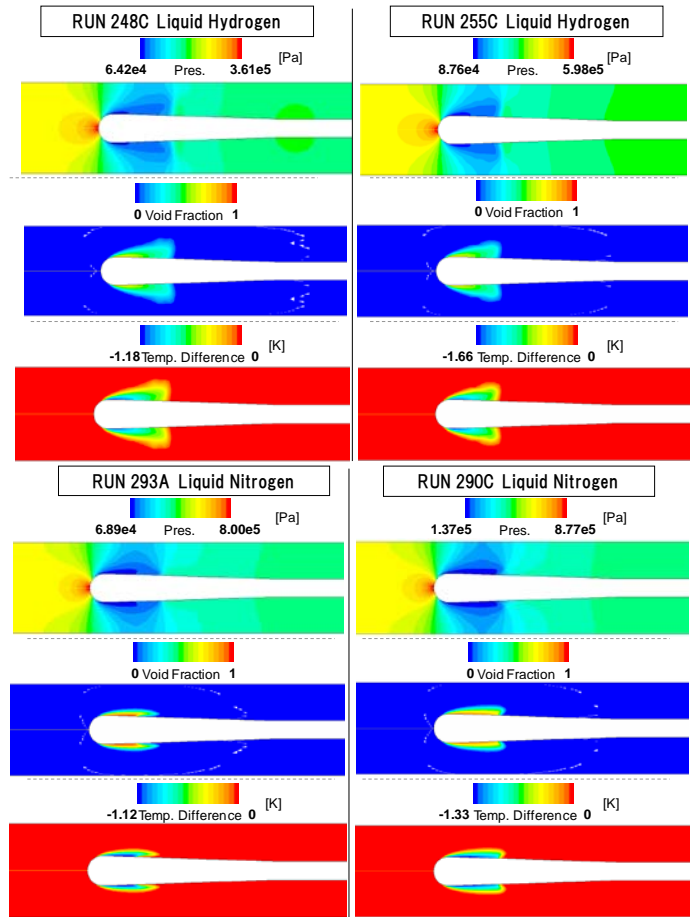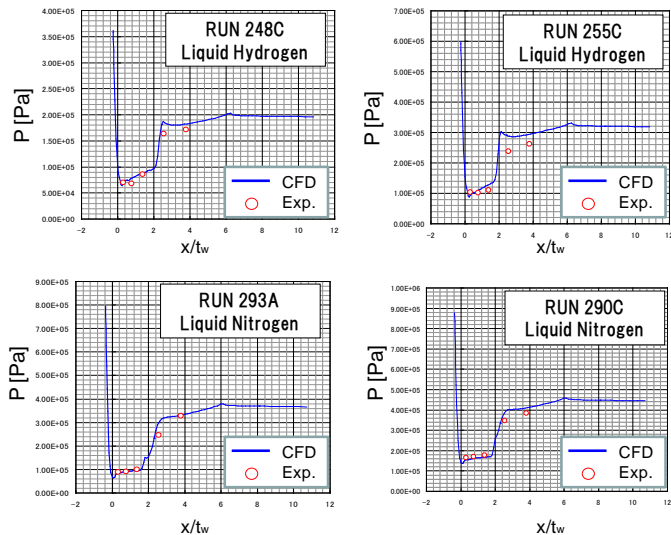


**Figure 13:** Contours of pressure, void fraction and temperature difference

The next validation objective is a Laval nozzle. Presently, two different shapes are used, which is shown in Fig.14. The shape A is axisymmetric and working fluid is liquid methane (LCH4), and the shape B is a two-dimensional and liquid nitrogen. Fluid Property is shown in Table 3. Figure 15 shows pressure distribution comparison, and each comparison shows quite well agreement.
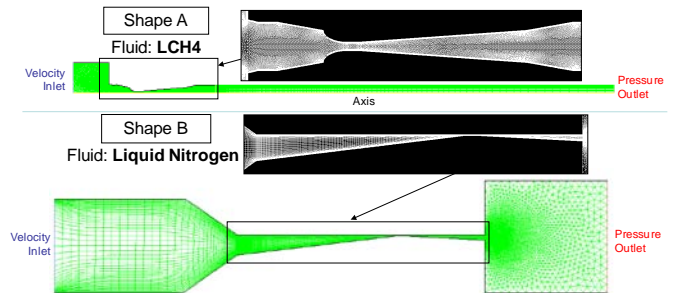


**Figure 14:** Shape and computational grid of Laval nozzles.

**Table 3:** Fluid property for Laval nozzle

**Liquid Methane (LCH4) 122K**

|  | Liquid Phase | Vapor Phase |
|---|---|---|
| Density [kg/m3] | 407. | 3.75 |
| $C_P$[J/kg/K] | $3.57 \times 10^3$ |  |
| Viscosity [Pa s] | $8.32 \times 10^{-5}$ | $4.92 \times 10^{-6}$ |
| Latent Heat [J/kg] | $4.90 \times 10^5$ | |
| $G_{sat}$[Pa/K] | 15490. | |
| $P_{sat}$[Pa] | $2.00 \times 10^5$ | |

**Liquid Nitrogen 95K**

|  | Liquid Phase | Vapor Phase |
|---|---|---|
| Density [kg/m3] | 713. | 24.0 |
| $C_P$[J/kg/K] | $2.23 \times 10^3$ |  |
| Viscosity [Pa s] | $9.85 \times 10^{-5}$ | $6.82 \times 10^{-6}$ |
| Latent Heat [J/kg] | $1.69 \times 10^5$ | |
| $G_{sat}$[Pa/K] | 41500. | |
| $P_{sat}$[Pa] | $5.84 \times 10^5$ | |
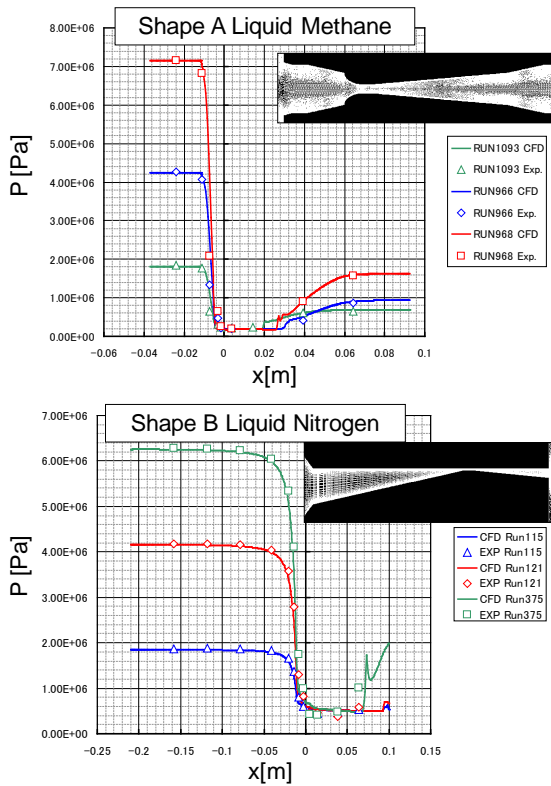


**Figure 15:** Pressure distribution comparison along the wall of the Laval nozzle

This section showed validation results of cryogenic fluid cavitation on the two-dimensional wing and the Laval nozzles, and it can be said that good agreement can be observed in each validation calculations. Present modeling of cavitation is based on a bubble cluster, and this means that void fraction should be small. According to the visualization of cryogenic cavitation[7], cavity does not shape large sheet cavitation, and it is a more mushy cavitation. The cavity formation is similar to the present

model, therefore, it can be considered that present validation showed good agreement.

## VALIDATION ON INDUCERS

As the final step, validation simulation on inducers was carried out. Inducer experiments with thermo-sensitive fluid are done by Yoshida, et al.[1] and Franc, et al.[18], and both of them shows that suction performance is improved and a cavity length becomes shorter than that of water. The objective of this validation calculation is to reproduce suction performance improvement in a cryogenic fluid by numerical simulation. Two inducers were chosen as validation objectives. Their shapes are shown in Fig.16. The inducer A is a front loading type inducer, which means pressure rise occurs around the leading edge. Usually, front loading type inducer has a large backflow region, and large tip-vortex and backflow vortex cavitation often occurs. The inducer B is an opposite design strategy, which is a aft loading type inducer. The tip-vortex and the backflow vortex cavitation becomes smaller than the front loading type one, but an interaction between tip vortex and the next blade is more likely to occur than the front loading type. Working fluids are room temperature water and 77K liquid nitrogen. Computational grid of each inducer is also shown in Fig.16. At the inlet, total pressure is set to be constant to adjust inlet cavitation number, and constant velocity condition is applied at the outlet to set mass flow rate. Since stagger angle of an inducer is large, grid generation by hexahedral mesh is difficult. Presently, tetrahedral mesh with prism layer was applied at the inducer part. Four prism layers were located on the inducer and casing surfaces, and this means that there are at least 9 grid layers in the tip clearance.
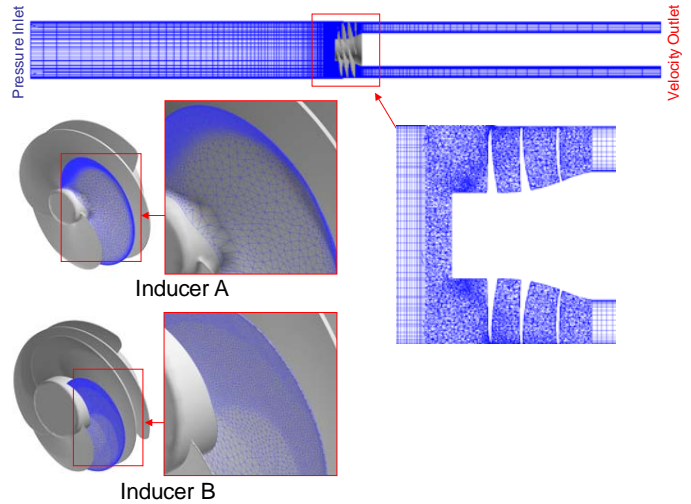


**Figure 16:** Shape and computational grid of two types of inducers.

Non-cavitating performance is compared as the first step. Figure 17 shows flow rate characteristic comparison about the inducer A and B in water. The inducer head agrees very well between experimental and numerical results. As the second step, suction performance is compared both in water and liquid nitrogen. The comparison is shown in Fig.18. According to this figure, both inducer A and B show suction performance

improvement in liquid nitrogen. Inducer B show good quantitative agreement, however, the tendency of suction performance of inducer A in liquid nitrogen is different, i.e. head is increased as cavitation number becomes low in experiment, on the contrary, computational head is decreased. It is considered that this difference is primarily derived from the backflow vortex cavitation, since the backflow vortex cavitation can be observed in the experiment, but this could not be captured in CFD (Fig.19). More detailed conservation should be done on the reason about the difference on the head drop tendency.
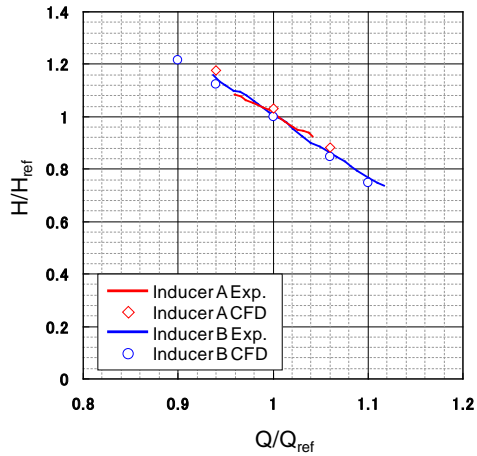


**Figure 17:** Head - Flow rate characteristic comparison under non-cavitating condition
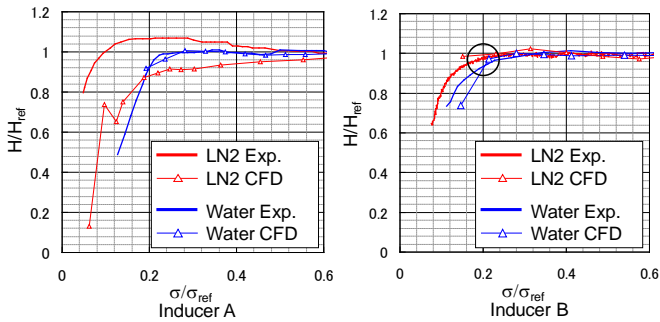


**Figure 18:** Suction performance comparison of each inducer. Circled point means a comparison point shown in Fig.20.
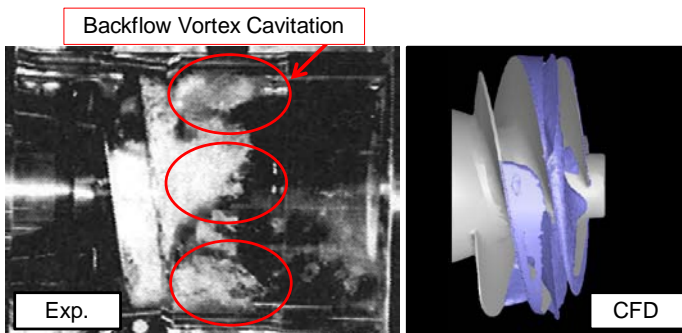


**Figure 19:** Backflow vortex cavitation by the experimental study and computed cavity shape of the inducer A

Internal flow is compared between water and liquid nitrogen about inducer B, since inducer B shows good quantitative agreement. Figure 20 shows void fraction comparison on the inducer blade on suction side at $\sigma/\sigma$ref=0.2, which point is shown by the circle in Fig.18. In liquid nitrogen, the cavity shape is almost identical to the water cavity, but void fraction becomes lower and cavity region is reduced. These tendencies are the same as the previous reports[18]. The restricted stream lines are also shown in Fig. 20. In water, radial bound streamline can be observed at the cavity closure region, on the contrary, such radial bound streamline is suppressed in liquid nitrogen. At the lower side of Figure 20 shows relative tangential velocity near the wall. The tangential velocity is suddenly reduced at the cavity closure region, but this velocity reduction becomes weaker in liquid nitrogen than in water. Low relative tangential velocity means fast tangential velocity in the absolute frame, and centrifugal force becomes large at high absolute tangential velocity. As a result, strong radial bound flow occurs in the water result. Generally speaking, sudden velocity decrease likely to introduce strong unsteadiness, in addition, remarkable spanwise flow may also introduce unsteady cavitation. Yoshida et al.[1] reported that unsteady cavitation became suppressed in cryogenic fluid, and Watanabe, et al.[19] showed that this suppression is derived by the change of the dynamic-transfer function by thermodynamic effect. The present result showed that internal flow becomes smoother in cryogenic fluid than in water, and this result indicates that unsteady cavitation may suppressed by the smooth internal flow. This means that the suppression of unsteady cavitation in cryogenic flow is not only by the change of the dynamic-transfer function but also the change of the internal flow.
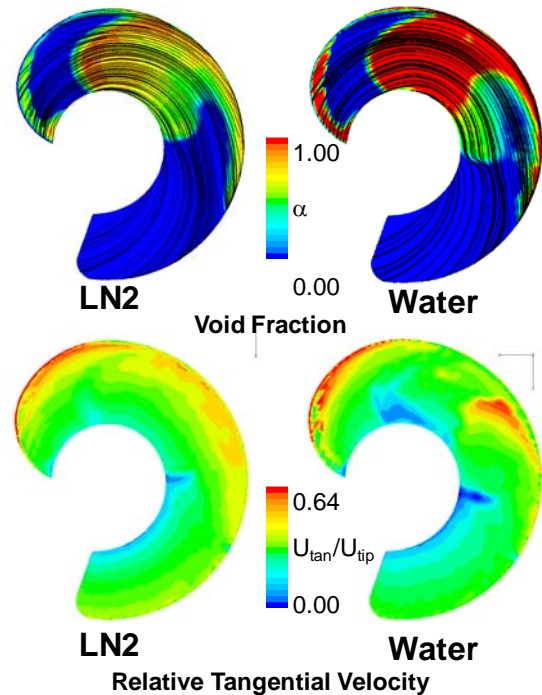


**Figure 20:** Void fraction and relative tangential velocity contours on the suction surface of the inducer B. Black lines show restricted streamlines.

## SUMMARY

In the present study, the cavitation model for cryogenic fluid, which is named Critical Radius Model, was established. The feature of this model is not to solve energy equation, therefore, this model is suitable to use design phase since computational cost becomes low. Several validation calculations both in water and in cryogenic fluid were carried out. The summary of the present study is as follows.

- The present cavitation model shows good result unless there is no strong separation or large scale cloud cavitation.
- The pressure distribution around the simple shape in cryogenic flow show good agreement.
- The suction performance improvement in cryogenic flow can be properly simulated by the present cavitation model.

The calculated result on the inducers implies that unsteady cavitation is suppressed in the cryogenic fluid. This point should be researched by conducting unsteady simulation.

## NOMENCLATURE

B: B-parameter
$C_e$: Evaporation Coefficient
$C_c$: Condensation Coefficient
$C_l$: Lift Coefficient $C_l = \dfrac{F_L}{\frac{1}{2}\rho_{liq} U_{inlet}^{2}}$

$C_d$: Drag Coefficient $C_d = \dfrac{F_D}{\frac{1}{2}\rho_{liq} U_{inlet}^{2}}$

$C_P$: Pressure Coefficient $C_P = \dfrac{P - P_{sat}}{\frac{1}{2}\rho_{liq} U_{inlet}^{2}}$

D: Blunt Body Diameter
F: Cavity Shedding Frequency
$F_D$: Drag Force
$F_L$: Lift Force
$F_{ST}$: Strouhal Number
f: Turbulent Viscosity Correlation Coefficient
$G_{sat}$: Gradient of Saturation Curve
H: Pump Head
k: Turbulent Kinetic Energy
L: Latent Heat
$L_{CAV}$: Maximum Cavity Length
N: Bubble Number Density
P: Pressure
$\Delta P_{turb}$: Apparent Saturation Pressure Change by Turbulence
$\Delta P_L$: Saturation Pressure Change by Latent Heat Absorption
Q: Volumetric Flow Rate
R: Bubble Radius
S: Bubble Surface Area

$\Delta T$: Temperature Decrease by Latent Heat Absorption
$\Delta T^*$: Analytical Temperature Decrease $\Delta T^* = \dfrac{\rho_{liq} L}{\rho_{vap} C_{Pliq}}$

t: Time
$t_w$: Thickness of the two-dimensional wing
$U_{inlet}$: Inlet Velocity
$U_{tan}$: Relative Tangential Velocity
$U_{tip}$: Tip Speed
**u**: Velocity Vector
X: Axial distance
α: Void Fraction (Gas Phase Volume Fraction)
χ: Quality (Gas Phase Mass Fraction)
$\mu_{turb}$: Modified Turbulent Viscosity
$\mu_{turbke}$: Turbulent Viscosity without Modify
ρ: Density
σ: Cavitation Number $\sigma = \dfrac{P_{ref} - P_{sat}}{\frac{1}{2}\rho_{liq} U_{inlet}^{2}}$

$\sigma_s$: Surface Tension

Suffix
sat: Saturation Condition
liq: Liquid Phase
vap: Vapor Phase
m: Gas-Liquid Mixture
ref: Reference

## REFERENCES

[1] Yoshida, Y., et al. , 2007, "Theremodynamic Effect on a Cavitating Inducer in Liquid Nitrogen," ASME, Journal of Fluids Engineering, Vol.129, No. 2.

[2] Deshpande, M., Feng, J. and Merkle, C.L. , 1997, : "Numerical Modeling of the Thermodynamic Effects of Cavitation", J. Fluids Eng., vol.119, pp.420-427.

[3] Tokumasu, T., Sekino, Y. and Kamijo, K., 2003, "A New Modeling of Sheet Cavitation Considering the Thermodynamic Effects," Proceedings of Fifth International Symposium on Cavitation(CD-ROM)

[4] Tani, N. and Nagashima, T. , 2002, "Numerical Analysis Of Cryogenic Cavitating Flow On Hydrofoil – Comparison Between Water and Cryogenic Fluids-," Proceedings of 4th International Symosium on Launcher Technology, #27 (CD-ROM).

[5] Hosangadi, H., and Ahuja, V. , 2006, "A Numerical Study of Cavitation in Cryogenic Fluids Part II; New Unsteady Model for Dense Cloud Cavitation,", Proceedings of Sixth International Symposium on Cavitation (CD-ROM).

[6] Frickha, S., Coutier-Delgosha, O. and Astolfi, J. A., 2009, "Numerical Investigations of the Cavitating Flow on Two-Dimensyonal Hydrofoils: Physical Modeling Methodologies," Proceedings of The 12th International Symposium on Transport Phenomena and Dynamics of Rotating Machinery, 20038(CD-ROM).

[7] Hord, J., 1973, "Cavitation in Liquid Cryogens II Hydrofoil," NASA CR2156

[8] Niiyama, K., 2008, "Study on Cavitation Instability in Subcooled Liquid Nitrogen Nozzle Flows," Tohoku University, A dissertation submitted for the degree of Doctor of Philosophy.

[9] Singhal, A. K., et al., 2002, "Mathematical Basis and Validation of the Full Cavitation Model," Journal of Fluids Engineering, Vol.124, pp.617-624

[10] Utturkar, Y., et al., 2005, "Recent Progress in Modeling of Cryogenic Cavitation for Liquid Rocket Propulsion," Progresss in Aerospace Sciences, Vol.41, p.p. 558-608

[11] Hord, J., 1973, "Cavitation in Liquid Cryogen," NASA CR-2242

[12] Brennen, C. R., 1995, "Cavitation and Bubble Dynamics," Oxford University Press.

[13] Rouse, H. and McNown, J.S., 1948, "Cavitation and Pressure Distribution: Head Forms at a Zero Angle of Yaw," Technical Report: State University of Iowa Engineering Bulletin, No.32.

[14] Numachi, F., et al., 1949, "Cavitation Tests of Six Profiles for Blade Elements,", Tohoku University, Institute of High Speed Mechanics Report, Vol.73, pp.25-46.

[15] Schnerr, G. H., 2003, "Modeling of Unsteady Cavitating Flows : Status and Future Development," Proceedings of 6th ISAIF, pp. K1-K21.

[16] Sakoda, M., et al, 2001, "Mechanism of cloud cavitation generation on a 2-D hydrofoil," CAVI2001, sessionA9, 2004 (CD-ROM).

[17] Simoneau, R. J. and Hendricks, R. C., 1979, "Two-Phase Choked Flow of Cryogenic Fluids in Converging-Diverging Nozzles," NASA Technical Paper 1484.

[18] Franc, J.-P., Rebattet, C. and Coulon, A., 2004, "An Experimental Investigation of Thermal Effects in a Cavitating Inducer," ASME J. Fluids Eng., Vol. 126, pp. 716-723.

[19] Watanabe, S., et al., 2008, "An Analysis of Thermodynamic Effect of Tip Leakage Vortex Cavitation," Proceedings of Cavitation Forum 2008 (CD-ROM).

[20] Kubota, A., Kato, H., and Yamaguchi, H., 1992, "A new modelling of cavitating flows---a numerical study of unsteady cavitation on a hydrofoil section," J. Fluid Mech., Vol.240, pp.59-96.